Alignment of symmetric top molecules by short laser pulses

Edward Hamilton and Tamar Seideman*
Department of Chemistry, Northwestern University, 2145 Sheridan Road, Evanston, Illinois 60208-3113, USA

Tine Ejdrup and Mikael D. Poulsen†
Department of Chemistry, University of Aarhus, DK-8000 Aarhus C, Denmark

Christer Z. Bisgaard and Simon S. Viftrup
Department of Physics and Astronomy, University of Aarhus, DK-8000 Aarhus C, Denmark

Henrik Stapelfeldt‡
Department of Chemistry, University of Aarhus, DK-8000 Aarhus C, Denmark
(Received 21 July 2005; published 20 October 2005)

Nonadiabatic alignment of symmetric top molecules induced by a linearly polarized, moderately intense picosecond laser pulse is studied theoretically and experimentally. Our studies are based on the combination of a nonperturbative solution of the Schrödinger equation with femtosecond time-resolved photofragment imaging. Using methyliodide and *tert*-butyliodide as examples, we calculate and measure the alignment dynamics, focusing on the temporal structure and intensity of the revival patterns, including their dependence on the pulse duration, and their behavior at long times, where centrifugal distortion effects become important. Very good agreement is found between the experimental and numerical results. This allows us to use our theory and numerical results to provide additional insight into the origin of the experimental findings.

DOI: 10.1103/PhysRevA.72.043402 PACS number(s): 42.50.Hz, 33.80.−b, 33.15.Bh, 42.65.Re

I. INTRODUCTION

Nonadiabatic alignment—alignment of neutral molecules by means of an intense laser pulse of short duration with respect to the natural system rotational time scales—has been a topic of rapidly increasing interest in recent years [1–7]. Although the approach was introduced [8] and numerically analyzed [9] a decade ago, it is only during the past 3–4 years that the first experiments were reported [10], enabling the realization of several intriguing applications. These include the use of alignment revivals to compress laser pulses [11], the phase control of rotational wave packets [12,13], the combination of alignment with attosecond pulse technology to map molecular orbitals [14], the application of nonadiabatic alignment to follow the time evolution of the electronic character of wave packets [15], and its use to manipulate the generation of high-order harmonics [16–20], to mention but a few.

Although most of the research on nonadiabatic alignment (also termed short-pulse alignment) has focused on diatomic and linear triatomic molecules, recent research suggests that polyatomic molecules offer much richer alignment dynamics, as well as a broad range of new potential applications. References [21–23] explore, experimentally and numerically, the nonadiabatic alignment of asymmetric top molecules, using iodobenzene and iodopentafluorobenzene as examples. Our motivation for extending these studies to explore other classes of molecules, in particular symmetric top rotors, is threefold. First, the rotations of rigid bodies in classical mechanics are qualitatively different for symmetric and asymmetric tops, the former being stable periodic and the latter unstable. One thus expects qualitatively different postpulse revival dynamics for these two classes of molecules, with several simplifications introduced in the higher-symmetry case. Second, the symmetric top system allows much more quantitative comparison of numerical and experimental results than has been possible in the past. Third, the Hamiltonian of the rigid symmetric top is in certain respects intermediate between that of the linear rotor, which has been the topic of numerous studies and is well understood, and that of the asymmetric top, which does not lend itself as readily to analytical interpretation but is typical of polyatomic molecules and hence interesting in the context of chemical applications.

In the present work we complement our previous work on the alignment dynamics of polyatomic molecules by exploring the nonadiabatic alignment of symmetric top molecules using similar experimental and theoretical approaches to those employed in Refs. [21–23]. We use the symmetric top example to explore also two problems that were not addressed in Refs. [21–23], namely, the effects of centrifugal distortion and the extent to which it can be characterized using alignment experiments, and the dependence of the alignment quality on the pulse duration under conditions that avoid nonresonant ionization [24,25]. The former problem was intensively studied within the related framework of rotational coherence spectroscopy [26] but is interesting to explore by comparison of observations to a nonperturbative

*Electronic address: seideman@chem.northwestern.edu
†Present address: Danish Technological Institute, Kongsvang Alle 29, DK-8000 Aarhus C, Denmark.
‡Electronic address: henriks@chem.au.dk

theory.[1] The latter problem is a matter of some practical relevance for obtaining the highest degree of alignment under field-free conditions.

In the next section we describe our theoretical and experimental methods. We start in Sec. II A with a discussion of the theory of nonadiabatic alignment dynamics of polyatomic molecules. Section II B outlines the numerical implementation of the theory. Our experimental technique has been discussed in detail in previous publications and hence is only briefly described here (Sec. II C). In Sec. III we present our experimental results for two symmetric top molecules, methyliodide and *tert*-butyliodide. We begin Sec. III with a description of our ion images (Sec. III A) and the way in which they translate into a rotational revival pattern (Sec. III B), and next present the observed centrifugal distortion and pulse duration effects (Sec. III C). Section IV applies the theory of Sec. II A to illustrate numerically several general properties of the nonadiabatic alignment of symmetric tops, and to generalize and interpret the experimental results of Sec. III. Our conclusions are summarized in Sec. V.

II. METHODS

Before proceeding to discuss our quantum-mechanical theory and the numerical and experimental methods, it is useful to provide reference to basic (although nontrivial) textbook material on the rotations of rigid bodies within classical mechanics. In particular we find illuminating the discussion of Landau and Lifshitz [27] regarding the regularity of the rotations of symmetric top molecules and its loss in the asymmetric top case. These features translate into a perfectly periodic revival structure in the postpulse evolution of symmetric top molecules, which is lost in the asymmetric case. We refer the reader also to an early classical trajectory study of the rotational fine structure of polyatomic molecules [28] and to several recent discussions of the classical mechanics of rigid rotors subject to external fields [29,30].

A. Theory

We consider an isolated molecular system subject to a linearly polarized nonperturbative radiation pulse,

$$\boldsymbol{\varepsilon}(t) = \frac{1}{2}[\boldsymbol{\varepsilon}(t)e^{i\omega t} + \boldsymbol{\varepsilon}^*(t)e^{-i\omega t}], \tag{1}$$

where $\boldsymbol{\varepsilon}(t)=\hat{\varepsilon}\varepsilon(t)$, $\hat{\varepsilon}$ is a unit vector in the field polarization direction, $\varepsilon(t)$ is an envelope function, and ω is the central frequency. In case the frequency is far detuned from vibronic transition frequencies, the field-matter interaction can be cast in the form of an approximate induced Hamiltonian [31,32]

$$H_{\mathrm{ind}} = -\frac{1}{4}\sum_{\rho\rho'} \varepsilon_\rho \alpha_{\rho\rho'} \varepsilon^*_{\rho'},$$

$$= \sum_{\rho} \varepsilon_\rho \mu^{\mathrm{ind}}_\rho, \quad \mu^{\mathrm{ind}}_\rho = \sum_{\rho'} \alpha_{\rho\rho'} \varepsilon^*_{\rho'}, \tag{2}$$

where $\rho=x,y,z$ are the space-fixed Cartesian coordinates, ε_ρ are the Cartesian components of the field, α is the polarizability tensor, and $\boldsymbol{\mu}^{\mathrm{ind}}$ defines an induced dipole operator. In terms of the body-fixed Cartesian coordinates $k=X,Y,Z$, the polarizability tensor takes the form

$$\alpha_{\rho\rho'} = \sum_{kk'} \langle \rho|k\rangle \alpha_{kk'} \langle k'|\rho'\rangle, \tag{3}$$

where $\langle k|\rho\rangle$ are elements of the transformation matrix between the space-fixed and body-fixed frames. Table 1 of Ref. [33] provides expressions for the $\langle k|\rho\rangle$ in terms of the Euler angles of rotation $\hat{R}=(\theta,\phi\chi)$, where $\theta=\cos^{-1}(\hat{z}\cdot\hat{Z})$ is the polar Euler angle, and ϕ and χ are the azimuthal angles of rotation about the space- and body-fixed quantization axes, respectively.

In the case of linearly polarized fields, the double sum in Eq. (2) collapses to a single term and the induced interaction takes the form,

$$\begin{aligned} H_{\mathrm{ind}} &= -\frac{\varepsilon^2(t)}{4}(\alpha^{ZX}\cos^2\theta + \alpha^{YX}\sin^2\theta\sin^2\chi + a_1) \\ &= -\frac{\varepsilon^2(t)}{4}\left(\frac{\alpha^{ZX}+\alpha^{ZY}}{3}D^2_{00}(\hat{R}) \right. \\ &\quad \left. -\frac{\alpha^{YX}}{\sqrt{6}}[D^2_{02}(\hat{R}) + D^2_{0-2}(\hat{R})] + a_2\right), \end{aligned} \tag{4}$$

where we followed the standard convention of defining the space-fixed z axis as the field polarization direction, $\hat{\varepsilon}_\rho=\hat{\varepsilon}_{\rho'}=\hat{z}$, and introduced generalized polarizability anisotropies as $\alpha^{ZX}=\alpha_{ZZ}-\alpha_{XX}$, $\alpha^{YX}=\alpha_{YY}-\alpha_{XX}$, α_{kk} being the body-fixed components of the polarizability tensor. The D^2_{qs} in the second equality are rotation matrices (often termed Wigner matrices) and we use the notation of Zare [34]. Whereas the first equality of Eq. (4) is useful for visualization purposes, the second will provide below an easy access to the form of the matrix elements of H_{ind} and the nature of the transitions it induces. The constants a_1 and a_2 in Eq. (4) merely shift the potential, without affecting the alignment dynamics, and are therefore omitted in what follows. The dependence of the interaction on θ and χ gives rise to the population of a broad wave packet in J and K spaces, J being the matter angular momentum and K the magnitude of the helicity (the eigenvalue of the projection of $\mathbf{J}$ onto the body-fixed z axis up to a factor $\hbar$). The lack of dependence of Eq. (4) on ϕ—the angle of rotation about the space-fixed z axis—leads to conservation of the magnetic quantum number M (the eigenvalue of the space-fixed z projection of $\mathbf{J}$ up to $\hbar$). In the case of a symmetric top molecule, $\alpha_{XX}=\alpha_{YY}$, and Eq. (4) simplifies as

$$H_{\mathrm{ind}} = -\frac{1}{4}\varepsilon^2(t)\Delta\alpha\cos^2\theta, \quad \Delta\alpha = \alpha_\parallel - \alpha_\perp, \tag{5}$$

where $\alpha_\parallel$ and $\alpha_\perp$ are the components of the polarizability tensor parallel and perpendicular to the molecular axis, re-

[1]Reference [1] includes centrifugal distortion in their numerical modeling of alignment of the N_2 and O_2 molecules.

spectively, $\alpha_{\parallel}=\alpha_{ZZ}$, $\alpha_{\perp}=\alpha_{XX}=\alpha_{YY}$. Due to the cylindrical symmetry of the molecule, the field-matter interaction is independent of χ. As a consequence, the projection of the angular momentum vector onto the top axis, the operator J_Z, remains well defined and the associated quantum number K remains a conserved quantum number in the presence of the field. Thus, a broad superposition of total angular momentum eigenstates is coherently excited during the pulse, while the z component of the angular momentum vector with respect to both the space- and the body-fixed frames is unaltered. Note that the interaction Hamiltonian takes the same form, Eq. (5) in the cases of linear and symmetric top molecules. Nonetheless, the nonradiative Hamiltonian (and hence also the alignment dynamics) differs, as will become evident below.

With the field-matter interaction given by Eqs. (2) and (3) [or by its special limit (4) or (5)], the complete Hamiltonian takes the form

$$H = H_{\mathrm{mol}} + H_{\mathrm{ind}} \tag{6}$$

in the strictly nonresonant case, where H_{mol} is the field-free molecular Hamiltonian. Within the rigid-rotor approximation H_{mol} reduces to the rotational Hamiltonian,

$$H_{\mathrm{mol}} \approx H_{\mathrm{rot}} = \frac{J_X^2}{2I_{XX}^e} + \frac{J_Y^2}{2I_{YY}^e} + \frac{J_Z^2}{2I_{ZZ}^e}, \tag{7}$$

where the operators J_k, $k=X,Y,Z$ are the Cartesian components of the total material angular momentum vector, I_{kk}^e are the corresponding principal moments of inertia, computed at the equilibrium configuration, and it is assumed that the body-fixed coordinate system has been chosen such that cross terms of the inertia tensor are eliminated.[2]

The rotational Hamiltonian is commonly expressed in terms of rotational constants; in energy units, $A_e=\hbar^2/2I_{aa}^e$, $B_e=\hbar^2/2I_{bb}^e$, $C_e=\hbar^2/2I_{cc}^e$, where I_{aa}^e, I_{bb}^e, and I_{cc}^e are the principal moments of inertia and, by convention, $I_{aa}^e \leqslant I_{bb}^e \leqslant I_{cc}^e$. In the case of prolate symmetric top rotors it is conventional to choose the body-fixed z axis as the a axis, whereby $\hbar^2 H_{\mathrm{rot}}=B_e\mathbf{J}^2+(A_e-B_e)J_Z^2$ with eigenvalues

$$E^{JK} = B_e J(J+1) + (A_e - B_e)K^2, \tag{8}$$

whereas in the oblate case choice of the c axis to define the body-fixed z axis is conventional, whereby $\hbar^2 H_{\mathrm{rot}} = B_e\mathbf{J}^2+(C_e-B_e)J_Z^2$ with eigenvalues

$$E^{JK} = B_e J(J+1) + (C_e - B_e)K^2. \tag{9}$$

In order to explore general aspects of nonadiabatic alignment, it is convenient to introduce molecule- and field-independent interaction, time, and temperature variables. We proceed by rewriting Eq. (6) with the general forms (4) and (7) for the radiative and nonradiative Hamiltonians as

$$\bar{H} = \sum_{k=X,Y,Z} \bar{B}_K \bar{J}_k^2 + \bar{\Omega}_R(\bar{\alpha}^{ZX}\cos^2\theta + \bar{\alpha}^{YX}\sin^2\theta\sin^2\chi), \tag{10}$$

where we define dimensionless Hamiltonian and angular momentum operators as

$$\bar{H} = \frac{\bar{I}H}{\hbar^2}, \quad \bar{I} = \frac{1}{2}(I_{XX}^e + I_{YY}^e),$$

$$\bar{J}_k = \frac{J_K}{\hbar}, \quad k = X,Y,Z, \tag{11}$$

respectively, and introduce dimensionless rotational constants, inertia components, and interaction parameters as

$$\bar{B}_k = \frac{\bar{I}}{2I_{kk}^e}, \quad \bar{\alpha}_k = \frac{\alpha_k}{\bar{\alpha}}, \tag{12}$$

and

$$\bar{\Omega}_R = \frac{\bar{I}\bar{\alpha}\varepsilon^2}{4\hbar^2}, \tag{13}$$

respectively. In Eqs. (10)–(13) $\bar{\alpha}$ is the trace of the polarizability tensor (the average polarizability), $\bar{\alpha}=(\alpha_{XX}+\alpha_{YY}+\alpha_{ZZ})/3$, and the generalized anisotropies $\bar{\alpha}^{kk'}=\bar{\alpha}_{kk}-\bar{\alpha}_{k'k'}$ are dimensionless versions of the analogous parameters introduced in Eq. (4). In terms of the Hamiltonian (10) the time dependent Schrödinger equation is transformed as

$$i\frac{\partial}{\partial\bar{t}}\Psi(\bar{t}) = \bar{H}\Psi(\bar{t}), \tag{14}$$

where $\bar{t}$ defines a dimensionless time variable

$$\bar{t} = \frac{\hbar}{\bar{I}}t. \tag{15}$$

The transformation of Eqs. (10)–(15) is structured such that the time variable will take a physical significance in the limit of a linear molecule, $\bar{t}=(2\pi/\tau_{\mathrm{rot}})t$, with transparent analogs in the prolate and oblate symmetric top cases (see below). Finally we introduce a reduced temperature variable as $\bar{T}=\bar{I}kT/\hbar^2$.

Our discussion so far pertains to the rigid-rotor limit. Deviations from perfect rigidity are expected at sufficiently long times, high intensities, and/or high temperatures for the effect of the coordinate dependence of the moments of inertia to leave its imprints on the rotational motion and distort it from perfect periodicity. This statement is quantified below and is illustrated experimentally and numerically in the following sections. We account for centrifugal distortion within the perturbative approach of Van Vleck that is standard in spectroscopy [34]. In the symmetric top limit, the rigid-rotor Hamiltonian is supplemented within this framework by the centrifugal distortion Hamiltonian

[2]Since the inertia tensor is Hermitian, there exists a transformation of the coordinates for which this tensor is diagonal [34,46].

$$\hbar^2 H_{\mathrm{CD}} = -D_J \mathbf{J}^4 - D_{JK} J_Z^2 \mathbf{J}^2 - D_K J_Z^4, \tag{16}$$

and the corresponding eigenvalues are modified to include a term

$$E_{\mathrm{CD}}^{JK} = -D_J [J(J+1)]^2 - D_{JK} J(J+1) K^2 - D_K K^4. \tag{17}$$

Denoting the symmetric top rigid-rotor eigenvalues of Eqs. (8) and (9) by E_{RR}^{JK}, we have that the time evolution of the rotational wave packet under field-free conditions (and hence the revival pattern) is determined by the coherent interference of energy phases of the general form $f^{JK} \exp[-i(E_{\mathrm{RR}}^{JK} + E_{\mathrm{CD}}^{JK})t/\hbar]$, where f^{JK} are time-independent coefficients. It follows that centrifugal distortion will have negligible effect as long as $t \ll \pi\hbar / E_{\mathrm{CD}}^{JK}$ but will dephase the rotational components and thus destroy the revival pattern for t of order $\pi\hbar / E_{\mathrm{CD}}^{JK}$. Clearly, high intensities enhance the rotational excitation and hence encourage centrifugal distortion, but the fact that rotational constants are typically orders of magnitude larger than distortion constants implies that several revivals would be observed before centrifugal distortion is discerned.

B. Numerical implementation

With the form of the Hamiltonian for the molecular symmetry in question identified, we proceed to solve the time-dependent Schrödinger equation subject to the nonperturbative interaction. The wave packet is expanded in a suitable rotational basis as

$$|\Psi_{\xi \mathbf{v} \mathbf{n}_i}(t)\rangle = \sum_{\mathbf{n}} C_{\xi \mathbf{v} \mathbf{n}_i}^{\mathbf{n}}(t) |\mathbf{n}\rangle, \tag{18}$$

where ξ and $\mathbf{v}$ are the electronic and vibrational indices (which are conserved) and $\mathbf{n}_i$ is the set of rotational quantum numbers of the parent state, which define the initial conditions. The dependence of the expansion coefficients on the initial state indices $\{\xi, \mathbf{v}, \mathbf{n}_i\}$ is indicated explicitly in Eq. (18) but omitted for clarity of notation in what follows, $C^{\mathbf{n}}(t) \equiv C_{\xi \mathbf{v} \mathbf{n}_i}^{\mathbf{n}}(t)$. To simplify the presentation we omit the conserved quantum numbers ξ and $\mathbf{v}$ also from the left-hand side, $\Psi_{\mathbf{n}_i} \equiv \Psi_{\xi \mathbf{v} \mathbf{n}_i}$. Substituting Eq. (18) in the time-dependent Schrödinger equation

$$i\hbar \frac{\partial \Psi(t)}{\partial t} = H(t) \Psi(t),$$

and using the orthonormality of the expansion basis states, one derives a set of coupled differential equations for the expansion coefficients,

$$\begin{aligned} i\hbar \dot{C}^{\mathbf{n}}(t) &= \sum_{\mathbf{n}'} \langle \mathbf{n} | H(t) | \mathbf{n}' \rangle C^{\mathbf{n}'}(t) \\ &= \sum_{\mathbf{n}'} [\langle \mathbf{n} | H_{\mathrm{rot}} | \mathbf{n}' \rangle + \langle \mathbf{n} | H_{\mathrm{ind}}(t) | \mathbf{n}' \rangle] C^{\mathbf{n}'}(t), \end{aligned} \tag{19}$$

where both the nonradiative and the radiative matrix elements are analytically solvable in the rotational basis.

In the case of a symmetric top molecule, it is convenient to use as an expansion basis the eigenstates of H_{rot}, $|\mathbf{n}\rangle = |JKM\rangle$,

$$\langle \hat{R} | JKM \rangle = \sqrt{\frac{2J+1}{8\pi^2}} D_{MK}^{J^*}(\hat{R}), \tag{20}$$

and the matrix elements in Eq. (19) take the form

$$\begin{aligned} &\langle JKM | H(t) | J'K'M' \rangle \\ &\quad = \delta_{KK'} \delta_{MM'} \left(E^{JK} \delta_{JJ'} - \frac{2}{3} \frac{\varepsilon^2(t) \Delta\alpha}{4} \langle JKM | D_{00}^2 | J'KM \rangle \right), \end{aligned} \tag{21}$$

where

$$\begin{aligned} \langle JKM | D_{qs}^2 | J'K'M' \rangle &= (-1)^{K'+M'} \sqrt{(2J+1)(2J'+1)} \\ &\quad \times \begin{pmatrix} J & 2 & J' \\ M & q & -M' \end{pmatrix} \begin{pmatrix} J & 2 & J' \\ K & s & -K' \end{pmatrix}. \end{aligned} \tag{22}$$

With the form of the wave packet determined via solution of the set of coupled differential equations (19), all observables of interest can be computed nonperturbatively as functions of time. Solution of the time-dependent Schrödinger equation with an initial condition $\mathbf{n} = \mathbf{n}_i$ produces observables $O_{\mathbf{n}_i}(t)$ corresponding to a pure state, that is, to an experiment where the parent state has been prepared in an eigenstate of the field-free Hamiltonian. Boltzmann-averaged observables $O_T(t)$, corresponding to experiments where the parent state is a mixed state defined by a rotational temperature, are obtained from the pure state analogs as

$$O_T(t) = \sum_{\mathbf{n}_i} w_{\mathbf{n}_i}(T_{\mathrm{rot}}) O_{\mathbf{n}_i}(t), \tag{23}$$

where $w_{\mathbf{n}_i}(T_{\mathrm{rot}})$ are normalized weight functions. The observable that is most commonly used to quantify the degree and the time evolution of the alignment is the expectation value of $\langle \cos^2 \theta \rangle$ in the wave packet,

$$\begin{aligned} \langle \cos^2 \theta \rangle_{\mathbf{n}_i}(t) &= \langle \Psi_{\mathbf{n}_i}(t) | \cos^2 \theta | \Psi_{\mathbf{n}_i}(t) \rangle \\ &= \sum_{\mathbf{n}\mathbf{n}'} C^{\mathbf{n}^*}(t) C^{\mathbf{n}'}(t) \langle \mathbf{n} | \cos^2 \theta | \mathbf{n}' \rangle \end{aligned} \tag{24}$$

with the corresponding thermally averaged observable $\langle \cos^2 \theta \rangle_T(t)$ determined through Eq. (23). Complementing this average in coordinate space is the expectation value of $\mathbf{J}^2$ in the wave packet,

$$\langle J^2 \rangle_{\mathbf{n}_i}(t) = \langle \Psi_{\mathbf{n}_i}(t) | \mathbf{J}^2 | \Psi_{\mathbf{n}_i}(t) \rangle = \sum_{\mathbf{n}} |C^{\mathbf{n}}(t)|^2 J(J+1), \tag{25}$$

which quantifies the extent of rotational excitation.

C. Experimental setup

The principle of the experiment as well as the experimental setup is similar to that used in our previous studies [22]; hence the description here is brief. The basic idea of the experiment is to align a sample of either methyliodide or *tert*-butyliodide molecules by a short laser pulse and measure the time-dependent degree of alignment. This is implemented in a three-step procedure. First, the molecules are irradiated

by an 800 nm pulse with a duration in the range from 0.5 to 3.0 ps and a peak intensity below the value where molecular ionization or multiphoton dissociation starts to occur. This pulse builds up a rotational wave packet that evolves in time subject to the field-free Hamiltonian; see Eq. (18). Second, the molecules are photodissociated through one photon absorption from a 266 nm pulse sent at a controllable delay with respect to the 800 nm pulse. The dissociation leads to formation of an iodine atom and a molecular radical in a direct bond-breaking process, causing the atomic iodine fragments to fly away in the direction of the molecular symmetry axis (threefold axis in either case). Thus, measurement of the molecular alignment, i.e., the spatial confinement of the C—I axis, is equivalent to measurement of the direction of the iodine photofragments. This is done by selective three-photon resonant ionization of either the I or the I^* atoms, by a 5-ns-long pulse, and projection of the I^+ ions onto a two-dimensional (2D) detector by weak static electric fields in an ion imaging geometry. The ns ionization pulse is delayed by ~12 ns with respect to the 800 and 266 nm pulses and it causes negligible changes in the trajectory of the iodine photofragments.

The 800 nm pulses are created by passing part of the output from an amplified Ti-sapphire femtosecond laser system through a home-built grating stretcher. The 266 nm pulses are created by third-harmonic generation in two beta barium borate crystals of another part of the output from the Ti-sapphire system. The resonant ionization pulses stem from the frequency-doubled output of a nanosecond dye laser pumped by the second harmonic of a nanosecond neodymium-doped yttrium aluminum garnet (Nd:YAG) laser. The wavelength of the ionization pulses is tuned to 304.59 nm such that the I ($^2P_{3/2}$) photofragments are measured. Alternatively, the wavelength can be set to 303.96 nm to probe the I^* ($^2P_{1/2}$) photofragments.

The molecular beam is formed by expanding ~10 mbar of methyliodide or ~2 mbar of *tert*-butyliodide[3] in either argon or helium through a 0.5-mm-diameter nozzle into vacuum. The backing pressure of argon is kept at 2 bar and the helium pressure at 3 bar. The molecular beam is skimmed twice and finally crossed at 90° by the three laser beams focused into the target vacuum chamber with a 30-cm-focal-length achromatic lens.

III. EXPERIMENTAL RESULTS

A. Ion images

Figure 1 shows four raw I^+ images recorded at different times with respect to a 0.75-ps-long alignment pulse of peak intensity 1.3×10^{13} W/cm^2 and using methyliodide, seeded in 2 bar argon, as the target molecule. The ion image recorded without the alignment pulse [Fig. 1(a)] exhibits two pairs of prominent half rings located in the outermost radial region. Their angular localization around the dissociation pulse polarization (vertical) is caused by the mainly parallel character of the electronic transition ($n\rightarrow\sigma^\star$ transition) that triggers dissociation [35]. The outermost half rings are due to ionization, by the 304 nm pulse, of the I atoms formed from photodissociation of CH_3I molecules with the 266 nm pulse. These rings are hereafter referred to as the 266 nm rings. Those molecules that are not dissociated by the 266 nm pulse may be dissociated by the (front of the) 304 nm pulse and, subsequently, the I fragments can be ionized by the (tail of the) same pulse. These I^+ ions give rise to the innermost half rings, hereafter referred to as the 304 nm rings. Their appearance at smaller radial distances than the 266 nm rings, corresponding to lower kinetic energies of the I^+ ions, is expected due to the lower photon energy of the 304 nm pulse compared to the 266 nm pulse.

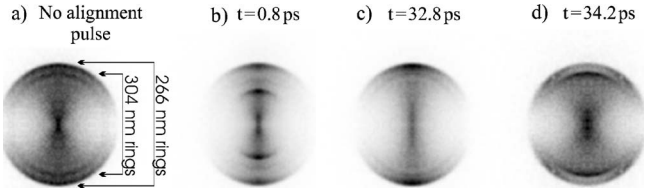

FIG. 1. I^+ images, from methyliodide molecules, recorded at different times t with respect to the peak of the alignment pulse (τ_{FWHM}=0.75 ps, $I_0=1.3\times10^{13}$ W/cm^2). (a) No alignment pulse present, t=(b) 0.8, (c) 32.8, and (d) 34.2 ps. Each image is accumulated over 10 000 laser shots. All three laser pulses are linearly polarized along the vertical axis.

The determination of the time-dependent alignment is based on the 266 nm rings. Since they are completely radially separated from the 304 nm rings there is no ambiguity in extracting $\langle\cos^2\theta\rangle$ using the radial region outside the 304 nm rings. The number of ion hits in the 304 nm rings is approximately the same in the four images shown in Fig. 1. The different appearance intensities of these 304 nm rings result from the fact that each image is scaled with respect to its most intense part.

When the 800 nm pulse is included, there is a strong angular confinement of the 266 nm rings shortly after the 800 nm pulse—illustrated by the t=0.8 ps image in Fig. 1(b). We identify this as alignment of the C—I axis of the methyliodide molecules. Hereafter, the alignment dephases in less than 5 ps and reaches a constant level out to the first half revival located, at around t=34 ps. Here, the alignment reaches a local maximum at t=32.8 ps [Fig. 1(c)] and a local minimum at t=34.2 ps [Fig. 1(d)]. We note that the image in Fig. 1(d) is less confined along the vertical axis than the image without the alignment pulse [Fig. 1(a)] indicating that the molecules are antialigned, i.e., confined to the plane perpendicular to the alignment axis.[4]

B. Rotational revivals

To quantify the alignment dynamics we recorded ion images in the range 1–75 ps from methyliodide seeded in 3 bar

[3]Helium or argon is bubbled through liquid methyliode at a temperature of ~−50 °C at which the vapor pressure is ~10 mbar, or through liquid *tert*-butyliodide at a temperature ~−30 °C where the vapor pressure is ~2 mbar.

[4]Due to the angular selectivity of the vertically polarized dissociation pulse (266 nm) the density of the 266 nm rings in Fig. 1(d) is highest at ~45°.

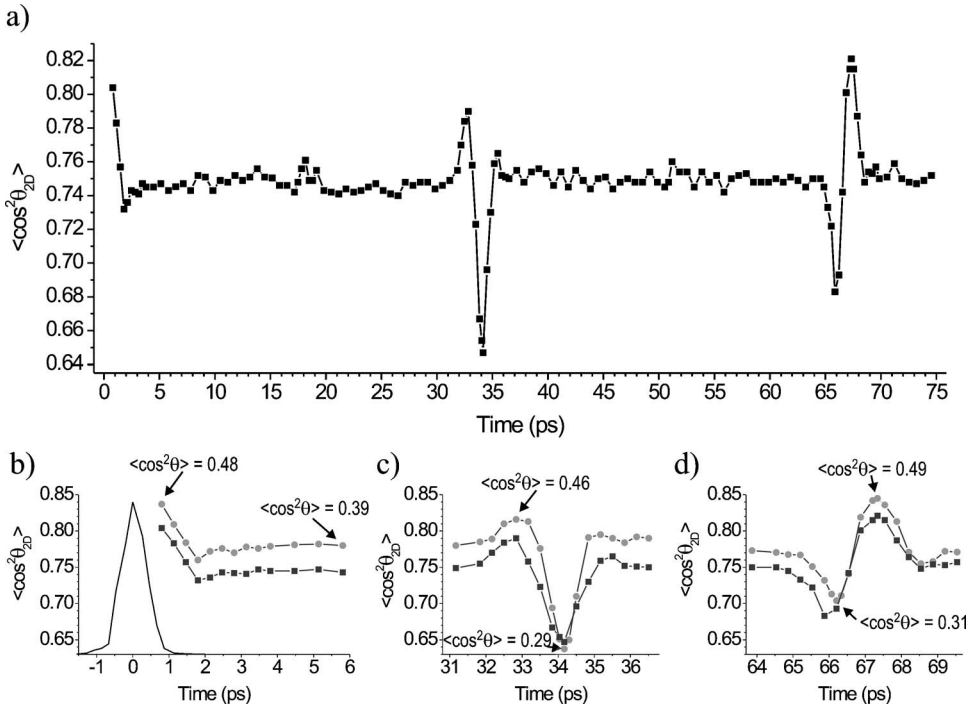

FIG. 2. Alignment dynamics of CH_3I molecules seeded in 3 bar helium, represented by $\langle \cos^2 \theta_{2D} \rangle$ as a function of time after the peak of the 800 nm alignment pulse (black squares). Lines between the points are included to guide the eye. (a) Long time scan; (b)–(d) magnified views of the three alignment transients. In (b)–(d) $\langle \cos^2 \theta_{2D} \rangle$ obtained for CH_3I seeded in 2 bar argon is also shown (gray circles). The $\langle \cos^2 \theta \rangle$ values are extracted from high-statistics ion images (of CH_3I seeded in argon) recorded at selected times, several of which are shown in Fig. 1. The cross-correlation trace of the alignment pulse, $\tau_{\mathrm{FWHM}}=0.75$ ps, $I_0=1.3\times10^{13}$ W/cm^2, is shown as a full curve in (b). Without the alignment pulse $\langle \cos^2 \theta_{2D} \rangle=0.71$.

helium. The alignment pulses were similar to those used to record the images in Fig. 1, i.e., 0.75 ps long and a peak intensity of $\sim 1.3\times10^{13}$ W/cm^2, which is just below the ionization threshold. From each image, accumulated over 2000 laser shots, we determined $\langle \cos^2 \theta_{2D} \rangle$, where θ_{2D} is the angle between the 800 nm polarization and the ion velocity in the detector plane [36]. The results are displayed in Fig. 2(a). The value of $\langle \cos^2 \theta_{2D} \rangle$ peaks shortly after the 800 nm pulse whereafter it quickly decreases and remains almost constant over the entire time interval except for two prominent, narrow transients located around 34 and 67 ps. These transients are identified as the first half and the first full rotational revivals, respectively. At the half revival the molecules initially align, then antialign, and finally return to the background level within a few picoseconds. At the full revival the order of the alignment dynamics is reversed, i.e., antialignment precedes alignment.

Figures 2(b)–2(d) show expansions of the alignment dynamics in the time intervals corresponding to the three alignment transients. In addition to the data from Fig. 2(a), representing CH_3I in 3 bar helium, the figure also shows data recorded from CH_3I seeded in 2 bar of argon (gray circles). The shapes of the alignment transients are very similar for the two conditions of the molecular beam, although the highest degree of alignment is obtained when CH_3I is expanded in argon. We ascribe this to the fact that argon as a carrier gas produces a lower rotational temperature of the CH_3I molecules, which leads to an enhanced degree of alignment [22].

In order to make comparison with our theory, and to provide a transferable measure of the alignment that is independent of the dissociation dynamics, it is necessary to determine $\langle \cos^2 \theta \rangle$ (see Sec. II B) from the data. The number of ions recorded in each image that underpins the $\langle \cos^2 \theta_{2D} \rangle$ data points displayed in Fig. 2 is not sufficiently high to that end. Consequently, we recorded high-statistics images, similar to those shown in Fig. 1, at the maxima and minima of the alignment curve. These numbers are indicated by arrows in Figs. 2(b)–2(d). The highest value of $\langle \cos^2 \theta \rangle$, 0.49, is measured at the maximum of the full revival ($t=65.34$ ps) and the lowest value, 0.29, at the minimum of the half revival ($t=34.17$ ps). By comparison, for a sample of nonaligned molecules $\langle \cos^2 \theta \rangle=0.33$. In Sec. IV we discuss and explain our experimental findings by comparing to calculated results obtained using the theory outlined in Sec. II A.

As discussed in Sec. II A, for symmetric tops the alignment maximum immediately after the pulse is precisely reconstructed at the subsequent full revivals in the rigid-rotor approximation, but centrifugal distortion spoils the perfect periodicity at times comparable to the inverse of E_{CD}^{JK} in Eq. (17). To investigate the imprint of centrifugal distortion on the revival spectrum, we recorded $\langle \cos^2 \theta_{2D} \rangle$ in the time intervals corresponding to the first, second, fourth, eighth, 16th, and 42nd full revivals. The results are displayed in Fig. 3.

The shapes of the first two revivals [Figs. 3(a) and 3(b)] are essentially identical. At the fourth revival the maximum value of $\langle \cos^2 \theta_{2D} \rangle$ has decreased from ~ 0.84 to ~ 0.82. At the eighth and the 16th revivals [Figs. 3(d) and 3(e)] a further small decrease is observed in the peak value of

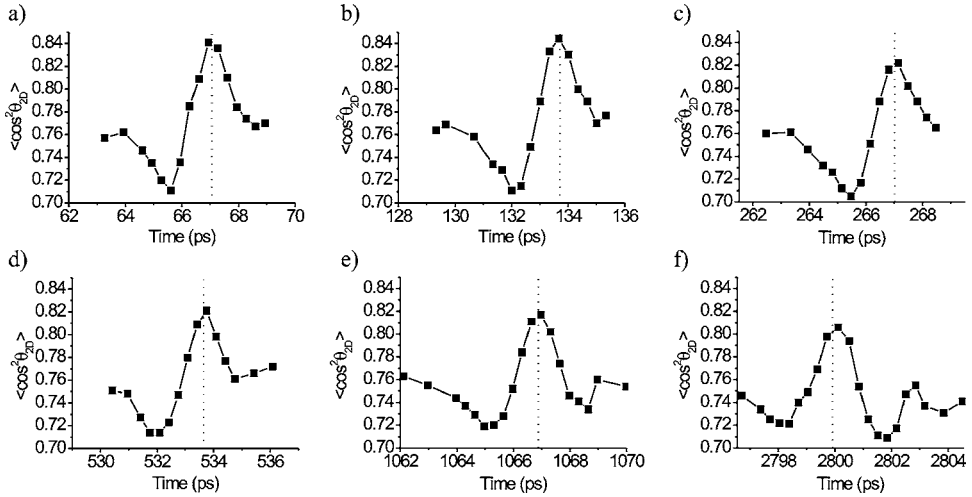

FIG. 3. Alignment dynamics of methyliodide seeded in 2 bar argon, represented by $\langle \cos^2 \theta_{2D} \rangle$, near selected full rotational revival times. The lines between the data points serve to guide the eye. (a) First, (b) second, (c) fourth, d) eighth, (e) 16th, and (f) 42nd full revivals. The dotted vertical lines indicate the predicted revival times $T_{\mathrm{rev}}=n/(2B)+0.4$ ps, n being the order of the revival. The addition of 0.4 ps to the integer multiple of the rotational time accounts for the appearance of the first alignment maximum 0.4 ps after the peak of the alignment pulse.

$\langle \cos^2 \theta_{2D} \rangle$. In addition, the modulation of the revival, i.e., the difference between the maximum and the minimum $\langle \cos^2 \theta_{2D} \rangle$ values has been reduced compared to the first two revivals. At the 42nd revival [Fig. 3(f)] the modulation is further reduced and the revival pattern is markedly distorted.[5] We ascribe the change in the revival shape to centrifugal distortion. Further details will be given in Sec. IV.

We also used our time-resolved photofragment imaging technique to record the alignment dynamics of another prolate symmetric top molecule, *tert*-butyliodide. The results, displayed in Fig. 4, show that the alignment dynamics and the revival structure are very similar to that of methyliodide. The alignment obtained immediately after the pulse quickly dephases to the level of the permanent alignment, where it remains approximately constant over the time interval investigated except for two narrow transients occurring close to 159.9 and 319.8 ps, corresponding to the half and full rotational revivals.[6]

C. Pulse duration effects

In general, for a molecular sample at a given rotational temperature the shape and the amplitude of the rotational revivals are determined by the intensity and the duration of the alignment pulse. In this subsection, we present selected experimental results on the dependence of the revival shape and strength on the pulse duration for both methyliodide and *tert*-butyliodide.

For CH_3I we measured the alignment dynamics around the first full revival for a set of different pulse durations at a fixed pulse energy. The pulse energy, ~ 120 μJ, was chosen such that the peak intensity of the shortest pulse was just below the value where multiphoton ionization sets in. As the duration is increased from 0.5 to 2.6 ps in Fig. 5 the peak intensity decreases from $\sim 1.6\times 10^{13}$ to $\sim 2.5\times 10^{12}$ W/cm^2. The strongest modulation of the revival, i.e., the largest difference between the maximum and the minimum $\langle \cos^2 \theta_{2D} \rangle$ value, is obtained for the shortest pulse [Fig. 5(a)] whereas the highest degree of alignment occurs for the 1.1 ps pulses [Fig. 5(c)]. Increasing the duration further [Figs. 5(d) and 5(e)] leads to a decrease in the maximum $\langle \cos^2 \theta_{2D} \rangle$ value as well as in the modulation.

The dependence of the alignment dynamics at the first full revival on the pulse duration was also investigated for *tert*-butyliodide. The results are shown in Fig. 6. For each of the three different pulse durations the peak intensity was set at the maximum value the molecule could withstand without ionizing. The dependence of the alignment on the pulse duration for *tert*-butyliodide is similar to that observed in the methyliodide case. The modulation of the degree of alignment is highest when the shortest pulse is used [Fig. 6(a)] whereas stronger alignment can be achieved by applying a longer pulse [Fig. 6(c)].

These experimental findings are generalized and explained in light of calculations in Sec. IV.

IV. NUMERICAL RESULTS AND COMPARISON WITH OBSERVATIONS

In this section we discuss our numerical results and use them to illustrate several of the features of the theory of Sec. II A, and to generalize and interpret the experimental results of Sec. III. We begin by illustrating a number of general properties of the nonadiabatic alignment of symmetric tops

[5]The maximum delay in our experimental setup, determined by a 50-cm-long delay stage, is about 3 ns. This defines the maximum revival order, 42, we could study here.

[6]In inverse time units, the B constant of *tert*-butyliodide is 1563.7 MHz—see Ref. [47]. The full revival time is then $1/(2B)=319.8$ ps.

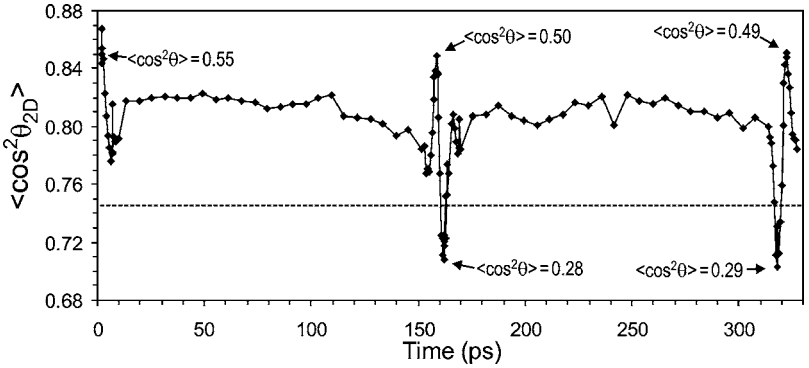

FIG. 4. Alignment of *tert*-butyliodide seeded in 3 bar helium (black diamonds connected by lines to guide the eye), represented by $\langle \cos^2 \theta_{2D} \rangle$ as a function of time after the peak of the alignment pulse ($\tau_{\mathrm{FWHM}}=1.3$ ps, $I_0=8.9\times10^{12}$ W/cm^2). The dashed horizontal line indicates $\langle \cos^2 \theta_{2D} \rangle$ without the alignment pulse. The $\langle \cos^2 \theta \rangle$ values are extracted from high-statistics ion images.

in a system-independent fashion, and proceed with numerical results for methyliodide. We use the reduced units introduced in Eqs. (10)–(15) in the first part, so as to keep the discussion system-independent, and conventional units in the second part, so as to allow comparison with experimental data.

Figure 7 investigates systematically the alignment dynamics of a rigid symmetric top [see Eqs. (8) and (9)] by varying the ratio of the inertia moments parallel and perpendicular to the symmetry axis, denoted R_B, from the prolate [Fig. 7(a)] through the spherical [Fig. 7(e)] to the oblate [Fig. 7(i)] limit. The polarizability tensor components are varied proportionately with the rotational constants so as to keep fixed the relation of the inertia and polarizability tensors. The interaction parameter of Eq. (13) is $\bar{\Omega}_R=1000$ and the temperature is $\bar{T}=2$. Figure 7(a), corresponding to the extreme prolate case, $R_B=I_{aa}/I_{bb}=1/2$, is readily understood by reference to the familiar revival structure of linear molecules. At integer multiples of the revival time that corresponds to rotation of the body-fixed z axis, $\bar{t}=2\pi n$, the initial alignment is precisely reconstructed, whereas at half revivals, $\bar{t}=2\pi(n+\frac{1}{2})$, the distribution is rotated by $\pi/2$. The new feature as compared to the linear case is the fine structure of the revival structure, arising from the second term in Eq. (8) and reflecting the availability of different orientations of the angular momentum vector with respect to the body-fixed frame. As the ratio of the two distinct inertia moments R_B approaches unity, the polarizability anisotropy decreases, the interaction strength falls, and the rotational periods about the two axes become comparable. Correspondingly, the fine structure is simplified [see Eq. (8)] and $\langle \cos^2 \theta \rangle$ decreases. In the spherical limit the polarizability tensor is isotropic, the interaction vanishes, and so do the rotational excitation and the alignment. The baseline of the revival pattern (the permanent alignment) approaches the linear molecule value of $\frac{1}{2}$ in the limit of small R_B and falls to the isotropic value of $\frac{1}{3}$ as $R_B \rightarrow 1$. As R_B is further increased, rotational excitation is restored, the structure of the revival spectrum reappears, and the baseline approaches $\frac{1}{2}$. The extreme oblate case, $R_B=I_{cc}/I_{bb}=2$, corresponding to the rotations of a disk, is illustrated in Fig. 7(i).

With the general features of the revival spectra of the symmetric top and their relation to the system properties established via the model illustrations, we proceed to apply the theory of Sec. II A to the CH_3I system of Sec. III. It is important to point out that quantitative comparison of the numerical and experimental results is not sought at present for several reasons. First, our experiments have insufficiently large statistical sets to extract $\langle \cos^2 \theta \rangle$, and hence in Sec. III we report a two-dimensional projection of the images, denoted $\langle \cos^2 \theta_{2D} \rangle$, which reproduces the temporal features of $\langle \cos^2 \theta \rangle$ but not its magnitude. Second, the experimental temperature is not known, and therefore our numerical calculations use a rough estimate of the temperature. Third, the focal spot size of the dissociation pulse in our experiment is comparable to that of the alignment pulse and hence the alignment at a distribution of intensities is recorded, rather

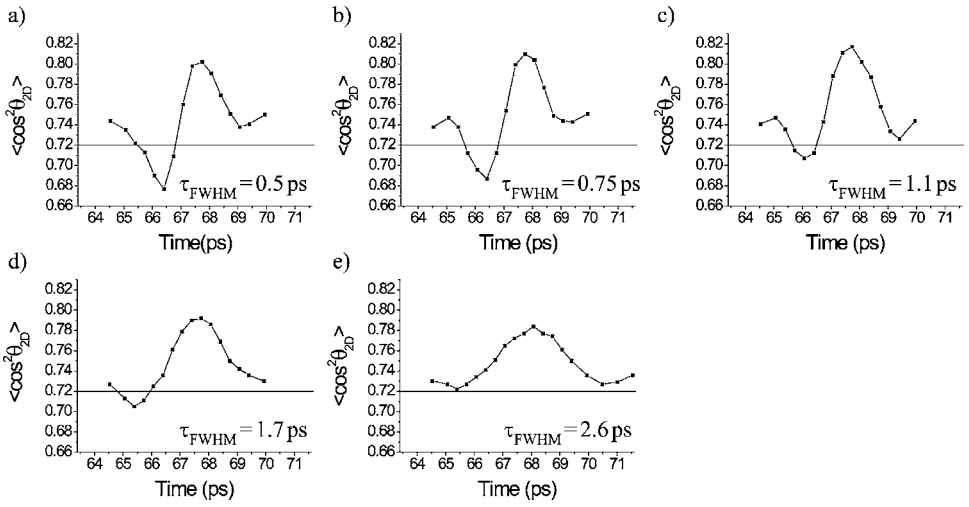

FIG. 5. $\langle \cos^2 \theta_{2D} \rangle$ for methyliodide seeded in 3 bar helium measured at the time interval of the first full revival for different durations of the alignment pulse. The lines through the data points serve to guide the eye. The energy of the alignment pulse is kept constant, yielding a peak intensity of $\sim 1.6\times10^{13}$ W/cm^2 for the 0.5 -ps-long pulse and $\sim 2.5\times10^{15}$ W/cm^2 for the 2.6-ps-long pulse. The horizontal lines indicate $\langle \cos^2 \theta_{2D} \rangle$ without the alignment pulse.

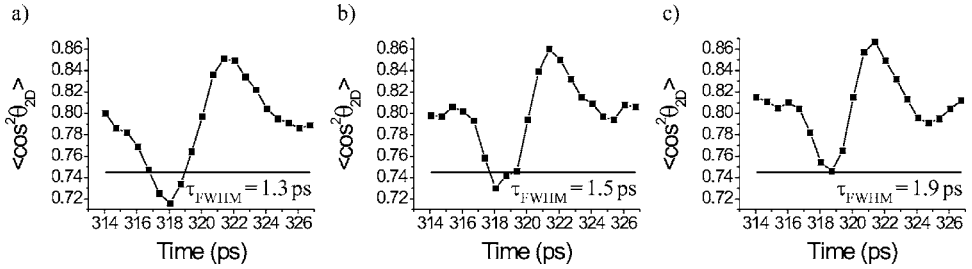

FIG. 6. $\langle \cos^2 \theta_{2D} \rangle$ for *tert*-butyliodide seeded in 3 bar helium measured at the time interval of the first full revival for different durations of the alignment pulse. The lines through the data points serve to guide the eye. (a) 1.3 ps, 8.9×10^{12} W/cm^2; (b) 1.5 ps, 8.1×10^{12} W/cm^2; (c) 1.9 ps, 6.8×10^{12} W/cm^2. The horizontal lines indicate $\langle \cos^2 \theta_{2D} \rangle$ without alignment pulse.

than the alignment at a single intensity. Numerically we account for the consequent intensity averaging by assuming that the alignment and dissociation pulses are concentric ellipsoids of identical orientation, each with a two-dimensional Gaussian profile, and using an experimentally determined value for the ratio of the spot sizes of the two fields, $\omega^{\text{probe}}/\omega^{\text{alignment}} \approx 0.7$. Our averaging procedure over the sampled intensities is independent of the absolute dimensions, but entails the assumption that both intensity profiles are Gaussian and is subject to the accuracy of the spot-size ratio. As shown below, for our present purpose this framework is perfectly adequate, but it is germane to keep in mind its limitations.

Figure 8 shows the predicted revival features for CH_3I, where we use a Gaussian pulse of duration and peak intensity identical to those of Fig. 2, and the same range of time delays between the alignment and dissociation pulses. While, as remarked above, quantitative comparison of the measured and numerical results is not our goal, the agreement of Fig. 8 with the experimental counterpart is gratifying. The calculation reproduces both the minor baseline alignment (permanent alignment) and the location and shape of the half- and full-revival transients, at 33 and 67 ps, respectively. (The former effect is well understood theoretically [37] and was illustrated experimentally in several studies of diatomic molecules.) Numerically we find somewhat higher maximum and lower minimum values of $\langle \cos^2 \theta \rangle$ than experimentally. This is likely due to the fact that the experimental dissociation probe technique used to measure the alignment tends to underestimate the maximum degree of alignment and overestimate the minimum degree of alignment [22]. Alternatively, this may indicate that we have underestimated the nonuniformity of the experimental intensity, and that a larger contribution of the alignment originates from molecules subject to less than the full peak intensity.

In Fig. 9, we study the variation of the revival shape and modulation as a function of the pulse duration and intensity at a constant total energy, in the same manner as in the experiments leading to Fig. 5. Figures 9(a)–9(e) show the expectation value of $\cos^2 \theta$ for the five sets of parameters studied experimentally in Figs. 5(a)–5(e). Our numerical and experimental results are in good agreement. More importantly, the theory provides insight into the content of the experimental figures, in particular the interesting observation that the strongest alignment modulation corresponds to the shortest alignment pulse [Fig. 5(a)], whereas the maximum alignment is observed for longer pulses [Figs. 5(b) and 5(c)]. The pulse-length dependence of the alignment under constant integrated pulse energy conditions can be understood by reference to Figs. 10(a)–10(e), where we provide the expectation value of $\mathbf{J}^2$ under the experimental parameters of Figs. 5(a)–5(e) [and Figs. 9(a)–9(e)], respectively. It is seen

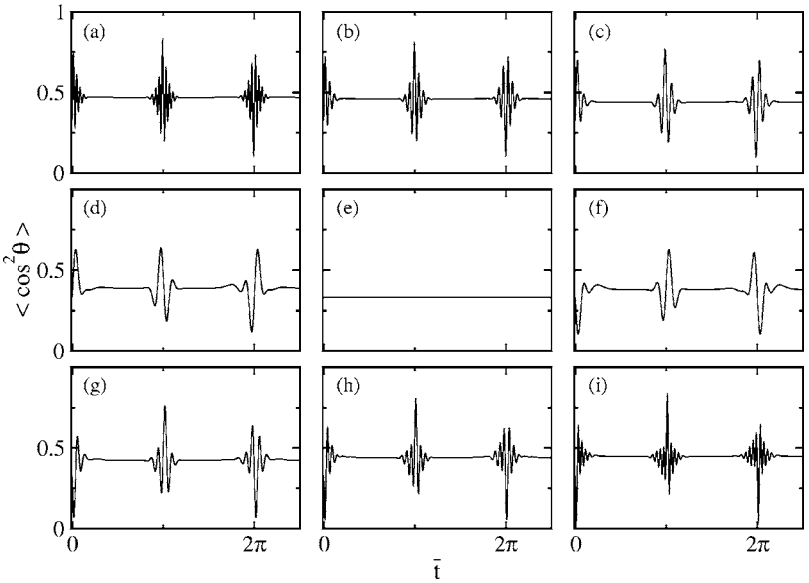

FIG. 7. Variation of the revival spectrum of a symmetric top rotor as a function of the ratio of the two distinct inertia moments R_B with the parameters varied in such a way as to hold the trace of the moment-of-inertia tensor constant. The polarizability tensor components are varied proportionately with the rotational constants. R_B=(a) 0.5, (b) 0.625, (c) 0.75, (d) 0.875, (e) 1 (spherical symmetry), (f) 1.14, (g) 1.33, (h) 1.6, and (i) 2.

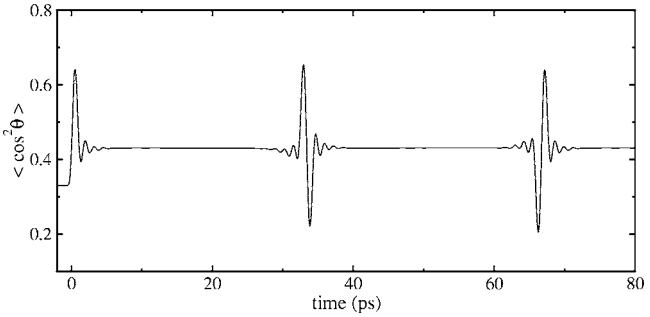

FIG. 8. Predicted alignment dynamics for CH_3I molecules at 10 K for alignment pulse parameters corresponding to Fig. 2, $\tau_{\mathrm{FWHM}}=0.75$ ps and $I_0=1.3\times10^{13}$ W/cm^2, using the alignment metric $\langle\cos^2\theta\rangle$. The calculation has been spatially averaged over a range of different intensities weighted with a spherical Gaussian distribution, to account for the effect of finite focal-spot sizes of the alignment and dissociation pulses.

that the short pulse of Fig. 5(a) leads to the highest degree of rotational excitation. The pulse of Fig. 5(b), however, establishes a better phase relation between the rotational components. For the pulse duration of Figs. 5(d) and 9(d) the dynamics deviates from the nonadiabatic limit, as is evident from the decrease of $\langle \mathbf{J}^2\rangle$ at the start of the pulse turnoff. This time dependence of $\langle \mathbf{J}^2\rangle$ reflects the decrease of the probabilities $|C^{n=J}|^2$ [see Eqs. (18) and (25)] corresponding to the highest-J components, in the course of the pulse turnoff, and hence the return of probability amplitude to the lower J levels. These dynamics lead to the deterioration of the alignment seen experimentally in Figs. 5(d) and 5(e) and numerically in Figs. 9(d) and 9(e). We note that the pulse energies used in the experiments were chosen so that the intensity is the maximum tolerable by CH_3I for the shortest-pulse case.

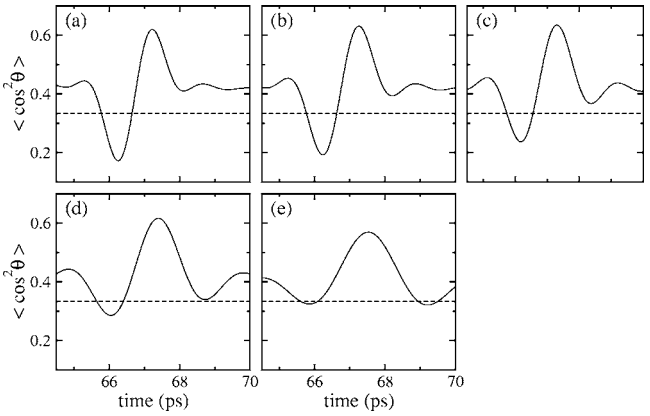

FIG. 9. Detailed alignment dynamics in the vicinity of the first full-revival transient for a range of pulse lengths and intensities, at constant total energy. The horizontal dotted line indicates the baseline for a rotationally isotropic sample in the absence of any alignment pulse, $\langle\cos^2\theta\rangle=1/3$. Panels (a)–(e) correspond in pulse parameters to panels (a)–(e) of Fig. 5, respectively. (a) $\tau_{\mathrm{FWHM}}=0.5$ ps, $I_0=1.6\times10^{13}$ W/cm^2; (b) $\tau_{\mathrm{FWHM}}=0.75$ ps, $I_0=1.067\times10^{13}$ W/cm^2; (c) $\tau_{\mathrm{FWHM}}=1.1$ ps, $I_0=7.273\times10^{12}$ W/cm^2; (d) $\tau_{\mathrm{FWHM}}=1.7$ ps, $I_0=4.706\times10^{12}$ W/cm^2; (e) $\tau_{\mathrm{FWHM}}=2.6$ ps, $I_0=3.077\times10^{12}$ W/cm^2.

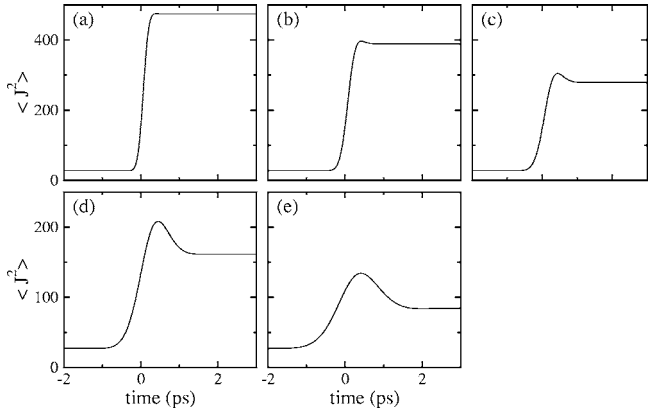

FIG. 10. Time evolution of the expectation value of the $\mathbf{J}^2$ operator in the wave packets of Fig. 9 during and immediately after the initial alignment pulse. Panels (a)–(e) correspond in pulse parameters to Figs. 9(a)–9(e) [and Figs. 5(a)–5(e)].

Since the nonresonant ionization depends nonlinearly on the intensity, the intensity used with the longer pulses is somewhat below the maximum tolerable and hence somewhat better alignment could be achieved.

The numerical results displayed in Figs. 7–9 were computed within the rigid-rotor approximation. We conclude this section by exploring the extent to which, and the mechanism through which, centrifugal distortion terms in the symmetric top Hamiltonian may leave imprints on the revival pattern at the temperature regime of interest. Our goals are to first confirm the argument of Sec. III that the deviation of the experimental alignment dynamics from periodicity are due to, and provide a means of characterizing, centrifugal distortion effects, and next to explore the way in which centrifugal distortion modifies the spectra. Figure 11 shows the revival spectra of CH_3I (with $D_J=7.95\times10^{-3}$ MHz and $D_{JK}=9.94\times10^{-2}$ MHz [38]) at the time ranges studied in Fig. 3, corresponding to the first, fourth, 16th, and 42nd full revivals. The solid curves account for centrifugal distortion whereas the dashed curves of Fig. 11 correspond to the rigid-rotor approximation. Comparison of the solid curves with the corresponding experimental spectra illustrates good agreement of the numerical and experimental results and confirms the argument of Sec. III. Comparison of the solid and dashed curves shows that centrifugal distortion effects are noticeable already at the fourth full revival and become important at nanosecond time scales. Nonetheless, the alignment is not severely degraded on the time scale probed here.

Centrifugal distortion destroys the perfect periodicity of the revival pattern by dephasing the wave-packet components (while coherence is fully maintained). On a qualitative level it can be considered the effect of several rotational manifolds with slightly different rotational constants that are in phase at short time but step out of phase as time progresses [see Eq. (17) and the discussion that follows]. A similar effect was numerically observed in time-resolved photoelectron angular distributions studies [39]. At times longer than considered here centrifugal distortion will lead to complete elimination of the revivals. Since we consider a discrete spectrum and a stable motion, the rotational compo-

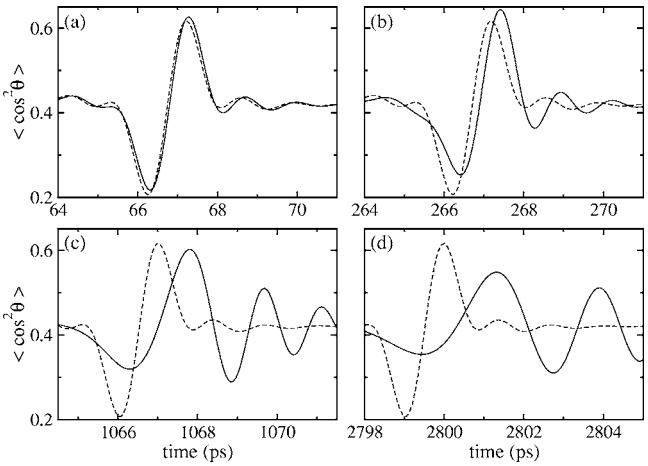

FIG. 11. Alignment dynamics of methyliodide at the temporal regimes of the low- and high-order revivals, illustrating the effect of centrifugal distortion on the revival shape and amplitude. (a) First, (b) fourth, (c) 16th, and (d) 42nd full revivals. The dashed curves omit the centrifugal distortion term in the Hamiltonian whereas the solid curves account for the complete Hamiltonian.

nents will rephase and the revival pattern observed on the time scale of a few rotational periods [Fig. 3(a)–3(c), 11(a), and 11(b) corresponding to 10^{-10} s time scales for CH_3I] will be once again reconstructed. Nonetheless, this rephasing will take place at times of the order of the inverse of the centrifugal constants ($1/2D_J \sim 63\ \mu s, 1/2D_{JK} \sim 5\ \mu s$), well beyond the time scales of experimental relevance to our study.

V. CONCLUSION

Our goal in the research reported in the previous sections has been to explore several problems in the nonadiabatic alignment of polyatomic molecules through the combination of time-resolved photofragment imaging experiments with a quantum-mechanical, nonperturbative theory. These include the revival pattern of polyatomic molecules at long times, where centrifugal distortion effects become non-negligible, the variation of the alignment dynamics with the pulse duration, as the field parameters are tuned from the nonadiabatic towards the adiabatic regime, and its variation with the molecular geometry as the inertia and polarizability tensors are altered from the linear and prolate through the spherical to the oblate and planar tops. Complementing previous research in this field, we focused on the case of symmetric top molecules, which is intermediate in certain respects between the linear and asymmetric top cases that were studied in the past. Our choice of systems allowed us to make more detailed comparison of our numerical and experimental observations than has been possible so far, leading to new insights into the origin of the experimental findings.

It is clear that much remains to be accomplished in the area of nonadiabatic, postpulse alignment of polyatomic systems. The potential of 3D alignment [40,41] in the polyatomic domain has been discussed in the recent literature [21,42]. Recent research on alignment in a dense gas [43], in solutions [44], and in solid materials [45] is expected to lead to increasing interest in nonadiabatic alignment, both as a control tool and as an analytical tool, with a growing variety of applications. Another avenue for future theoretical and experimental research is the combination of alignment with molecular optics—the application of strong field gradients to manipulate the center-of-mass motion of molecules.

ACKNOWLEDGMENTS

We acknowledge excellent support from Jan Thøgersen and from the technical staff members at the Department of Chemistry and the Department of Physics and Astronomy, University of Aarhus. T.S. is grateful to the U.S. Department of Energy (Grant No. DE-FG02-04ER15612) for support of this research. H.S. is grateful to the Carlsberg Foundation, The Lundbeck Foundation and the Danish Natural Science Research Council for support.

[1] P. W. Dooley, I. V. Litvinyuk, K. F. Lee, D. M. Rayner, M. Spanner, D. M. Villeneuve, and P. B. Corkum, Phys. Rev. A **68**, 023406 (2003).
[2] V. Renard, M. Renard, A. Rouzee, S. Guèrin, H. R. Jauslin, B. Lavorel, and O. Faucher, Phys. Rev. A **70**, 033420 (2004).
[3] K. F. Lee, I. V. Litvinyuk, P. W. Dooley, M. Spanner, D. M. Villeneuve, and P. B. Corkum, J. Phys. B **37**, L43 (2004).
[4] M. Leibscher, I. S. Averbukh, and H. Rabitz, Phys. Rev. A **69**, 013402 (2004).
[5] J. Ortigoso, Phys. Rev. Lett. **93**, 073001 (2004).
[6] V. G. Stavros, E. Harel, and S. R. Leone, J. Chem. Phys. **122**, 064301 (2005).
[7] D. Daems, S. Guerin, D. Sugny, and H. R. Jauslin, Phys. Rev. Lett. **94**, 153003 (2005).
[8] T. Seideman, J. Chem. Phys. **103**, 7887 (1995).
[9] J. Ortigoso, M. Rodriguez, M. Gupta, and B. Friedrich, J. Chem. Phys. **110**, 3870 (1999).
[10] F. Rosca-Pruna and M. J. J. Vrakking, Phys. Rev. Lett. **87**, 153902 (2001).
[11] R. A. Bartels, N. L. Wagner, M. D. Baertschy, J. Wyss, M. M. Murnane, and H. C. Kapteyn, Opt. Lett. **28**, 346 (2003).
[12] M. Spanner, E. A. Shapiro, and M. Ivanov, Phys. Rev. Lett. **92**, 093001 (2004).
[13] K. F. Lee, D. M. Villeneuve, P. B. Corkum, and E. A. Shapiro, Phys. Rev. Lett. **93**, 233601 (2004).
[14] J. Itatani, J. Levesque, D. Zeidler, H. Niikura, H. Pepin, J. C. Kieffer, P. B. Corkum, and D. M. Villeneuve, Nature (London) **432**, 867 (2004).
[15] T. Seideman, Annu. Rev. Phys. Chem. **53**, 41 (2002).
[16] V. Averbukh, O. E. Alon, and N. Moiseyev, Phys. Rev. A **64**, 033411 (2001).
[17] R. de Nalda, E. Heesel, M. Lein, N. Hay, R. Velotta, E. Springate, M. Castillejo, and J. P. Marangos, Phys. Rev. A **69**, 031804(R) (2004).

[18] M. Kaku, K. Masuda, and K. Miyazaki, Jpn. J. Appl. Phys. **43**, L591 (2004).
[19] A. D. Bandrauk and H. Lu, Int. J. Quantum Chem. **99**, 431 (2004).
[20] T. Kanai, S. Minemoto, and H. Sakai, Nature (London) **435**, 470 (2005).
[21] E. Péronne, M. D. Poulsen, C. Z. Bisgaard, H. Stapelfeldt, and T. Seideman, Phys. Rev. Lett. **91**, 043003 (2003).
[22] E. Peronne, M. D. Poulsen, H. Stapelfeldt, C. Z. Bisgaard, E. Hamilton, and T. Seideman, Phys. Rev. A **70**, 063410 (2004).
[23] M. D. Poulsen, E. Péronne, H. Stapelfeldt, C. Z. Bisgaard, S. S. Viftrup, E. Hamilton, and T. Seideman, J. Chem. Phys. **121**, 783 (2004).
[24] F. Rosca-Pruna and M. J. J. Vrakking, J. Chem. Phys. **116**, 6567 (2002).
[25] F. Rosca-Pruna and M. J. J. Vrakking, J. Chem. Phys. **116**, 6579 (2002).
[26] C. Riehn, Chem. Phys. **283**, 297 (2002).
[27] L. D. Landau and E. M. Lifshitz, *Mechanics* (Pergamon Press, Oxford, 1976).
[28] W. Harter and C. Patterson, J. Chem. Phys. **80**, 4241 (1984).
[29] C. A. Arango, W. W. Kennerly, and G. S. Ezra, J. Chem. Phys. **122**, 184303 (2005).
[30] K. Na and L. E. Reichl, Phys. Rev. A **72**, 013402 (2005).
[31] T. Seideman, J. Chem. Phys. **111**, 4397 (1999).
[32] P. S. Pershan, J. P. van der Ziel, and L. D. Malmstrom, Phys. Rev. **143**, 574 (1966).
[33] T. Seideman, Chem. Phys. Lett. **253**, 279 (1996).
[34] R. N. Zare, *Angular Momentum* (Wiley, New York, 1988).
[35] R. O. Loo, G. E. Hall, H. P. Haerri, and P. L. Houston, J. Phys. Chem. **92**, 5 (1988).
[36] J. J. Larsen, H. Sakai, C. P. Safvan, I. Wendt-Larsen, and H. Stapelfeldt, J. Chem. Phys. **111**, 7774 (1999).
[37] T. Seideman, Phys. Rev. Lett. **83**, 4971 (1999).
[38] J. W. Simmons and W. E. Anderson, Phys. Rev. **80**, 338 (1950).
[39] S. C. Althorpe and T. Seideman, J. Chem. Phys. **110**, 147 (1999).
[40] J. J. Larsen, K. Hald, N. Bjerre, H. Stapelfeldt, and T. Seideman, Phys. Rev. Lett. **85**, 2470 (2000).
[41] J. G. Underwood, B. J. Sussman, and A. Stolow, Phys. Rev. Lett. **94**, 143002 (2005).
[42] H. Stapelfeldt and T. Seideman, Rev. Mod. Phys. **75**, 543 (2003).
[43] S. Ramakrishna and T. Seideman, Phys. Rev. Lett. **95**, 113001 (2005).
[44] J. Ohkubo, T. Kato, H. Kono, and Y. Fujimura, J. Chem. Phys. **120**, 9123 (2004).
[45] T. Kiljunen, B. Schmidt, and N. Schwentner, Phys. Rev. Lett. **94**, 123003 (2005).
[46] E. B. Wilson, J. C. Decius, and P. M. Cross, *Molecular Vibrations* (Dover, New York, 1980).
[47] J. Q. Williams and W. Gordy, J. Chem. Phys. **18**, 994 (1950).